Molecular Cell

A Metabolic Basis for Endothelial-to-Mesenchymal Transition

Graphical Abstract
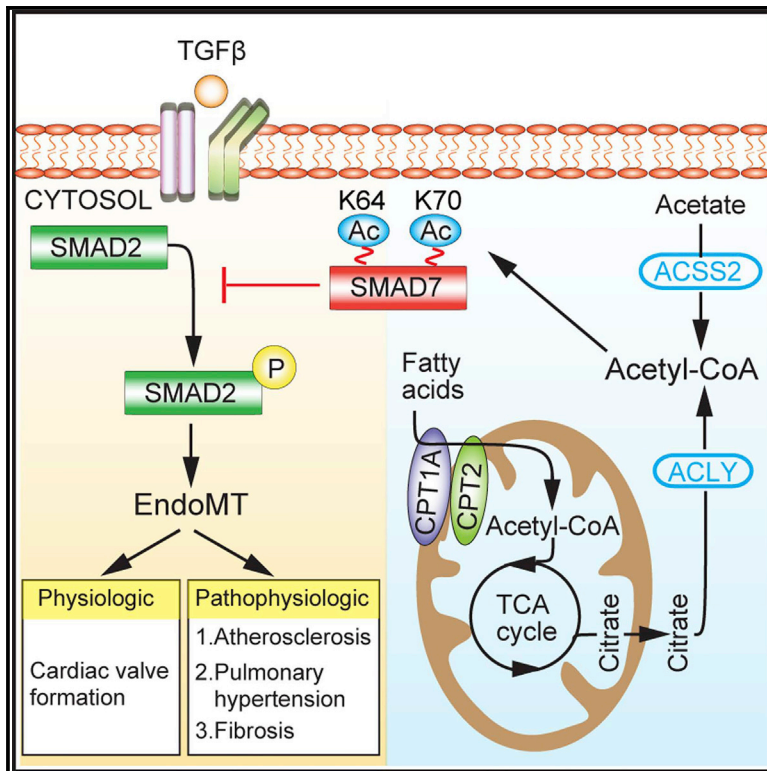
Authors

Jianhua Xiong, Hiroyuki Kawagishi, Ye Yan, ..., Michael J. Jurczak, Joshua P. Fessel, Toren Finkel

Correspondence

finkelt@pitt.edu

In Brief

Xiong et al. demonstrate that endothelial fatty acid oxidation (FAO) is a critical *in vitro* and *in vivo* regulator of endothelial-to-mesenchymal transition (EndoMT) and that therapeutic manipulation of endothelial metabolism could provide the basis for treating a growing number of EndoMT-linked pathological conditions.

Highlights

- Induction of EndoMT triggers a reduction in FAO

- FAO is required to maintain endothelial acetyl-CoA levels

- FAO modulates *in vitro* and *in vivo* EndoMT

A Metabolic Basis
for Endothelial-to-Mesenchymal Transition

Jianhua Xiong,[1] Hiroyuki Kawagishi,[1] Ye Yan,[1] Jie Liu,[1,7] Quinn S. Wells,[2] Lia R. Edmunds,[3] Maria M. Fergusson,[1] Zu-Xi Yu,[4] Ilsa I. Rovira,[1] Evan L. Brittain,[2] Michael J. Wolfgang,[5] Michael J. Jurczak,[3] Joshua P. Fessel,[6] and Toren Finkel[1,7,8,*]

[1]Center for Molecular Medicine, National Heart, Lung and Blood Institute, NIH, Bethesda, MD 20892, USA
[2]Department of Medicine, Division of Cardiovascular Medicine and Vanderbilt Translational and Clinical Cardiovascular Research Center, Vanderbilt University School of Medicine, Nashville, TN 37232, USA
[3]Department of Medicine, Division of Endocrinology and Metabolism, University of Pittsburgh School of Medicine, Pittsburgh, PA 15261, USA
[4]Pathology Core, National Heart, Lung and Blood Institute, NIH, Bethesda, MD 20892, USA
[5]Department of Biological Chemistry, Johns Hopkins University School of Medicine, Baltimore, MD 21205, USA
[6]Department of Medicine, Division of Allergy, Pulmonary and Critical Care Medicine, Vanderbilt University School of Medicine, Nashville, TN 37232, USA
[7]Aging Institute, Department of Medicine, University of Pittsburgh School of Medicine, Pittsburgh, PA 15261, USA
[8]Lead Contact
*Correspondence: finkelt@pitt.edu
https://doi.org/10.1016/j.molcel.2018.01.010

SUMMARY

Endothelial-to-mesenchymal transition (EndoMT) is a cellular process often initiated by the transforming growth factor β (TGF-β) family of ligands. Although required for normal heart valve development, deregulated EndoMT is linked to a wide range of pathological conditions. Here, we demonstrate that endothelial fatty acid oxidation (FAO) is a critical *in vitro* and *in vivo* regulator of EndoMT. We further show that this FAO-dependent metabolic regulation of EndoMT occurs through alterations in intracellular acetyl-CoA levels. Disruption of FAO via conditional deletion of endothelial carnitine palmitoyltransferase II ($Cpt2^{E-KO}$) augments the magnitude of embryonic EndoMT, resulting in thickening of cardiac valves. Consistent with the known pathological effects of EndoMT, adult $Cpt2^{E-KO}$ mice demonstrate increased permeability in multiple vascular beds. Taken together, these results demonstrate that endothelial FAO is required to maintain endothelial cell fate and that therapeutic manipulation of endothelial metabolism could provide the basis for treating a growing number of EndoMT-linked pathological conditions.

INTRODUCTION

EndoMT is a specific form of epithelial-to-mesenchymal transition (EMT) characterized by the loss of endothelial features and the acquisition of mesenchymal, fibroblast, or stem-cell-like characteristics (Kovacic et al., 2012; Sanchez-Duffhues et al., 2016). This process was initially described in the context of endocardial differentiation and it is now apparent that EndoMT contributes to the formation of the atrioventricular cushion, septa, and valves during normal cardiac development (Eisenberg and Markwald, 1995). While linked to physiological cardiac development, abnormal EndoMT has also been implicated in a growing number of pathological conditions. These include pulmonary hypertension (Stenmark et al., 2016), vein graft failure (Cooley et al., 2014), metastatic spread of tumors (Magrini et al., 2014; Potenta et al., 2008), atherosclerosis (Chen et al., 2015; Evrard et al., 2016), and fibrosis in key organs such as the heart and kidney (Piera-Velazquez et al., 2011; Zeisberg et al., 2007, 2008). Although transforming growth factor β (TGF-β) signaling is a potent inducer of EndoMT (Sanchez-Duffhues et al., 2016), the intracellular metabolic mediators regulating this process within endothelial cells are incompletely characterized.

Although proliferating endothelial cells rely primarily on glycolysis (De Bock et al., 2013), a recent study demonstrated that this cell type also requires fatty acid oxidation (FAO) (Schoors et al., 2015). Indeed, the mitochondrial-dependent, β-oxidation of long-chain fatty acids (LCFAs) is central to energy homeostasis in a wide array of cells (Houten et al., 2016). For successful transport from the cytosol into the mitochondrial matrix, LCFAs must undergo two successive enzymatic reactions, a sequence of events known as the carnitine shuttle. These reactions involve CPT1, located on the outer mitochondrial membrane, followed by CPT2, located on the inner mitochondrial membrane (Bonnefont et al., 2004). As such, the sequential activity of both CPT1 and CPT2 are required to import and hence, metabolize LCFA.

Here, we demonstrate a novel role for endothelial FAO in restraining EndoMT. In particular, we show that TGF-β signaling-induced EndoMT is accompanied by an inhibition of FAO. Furthermore, FAO inhibition potentiates EndoMT through regulation of intracellular acetyl-CoA levels and SMAD7 signaling. We further show that genetic disruption of $Cpt2$ modulates *in vivo* EndoMT. Together, these results establish endothelial FAO as an important regulator of the EndoMT process.

RESULTS

Induction of EndoMT Is Accompanied by a Reduction in FAO

Based on a previous strategy (Rieder et al., 2011), we found that primary cultures of human pulmonary microvascular endothelial cells (HPMVECs) could be stimulated to undergo EndoMT by treating these cells with a cytokine combination of TGF-β1 and interleukin-1β (IL-1β). These cytokine-treated endothelial cells underwent a clear morphological transition adopting a more fibroblast or mesenchymal appearance (Figure 1A). Coincident with this morphological switch, cytokine treatment of endothelial cells induced a host of mesenchymal markers, as well as a simultaneous decrease in endothelial markers (Figures 1B, S1A, and S1B). To investigate potential novel mediators of EndoMT, we performed a metabolomics profile using this *in vitro* system. This analysis revealed that EndoMT was accompanied by a rise in certain short chain acylcarnitines and a fall in glycolytic and tricarboxylic acid (TCA) cycle-linked organic acid metabolites (Figure 1C). This suggested that EndoMT might potentially involve a shift in the relative role of fatty acid and carbohydrate metabolism. Interestingly, upon induction of EndoMT, cytokine treatment induced an early decline in the level of CPT1A, the enzyme that plays a rate-limiting and obligate role in FAO (Figures 1D, S1C, and S1D). This decline in CPT1A expression is transient but specific (e.g., does not include CPT2) and precedes the induction of various mesenchymal markers (Figures S1E–S1H). This reduction of CPT1A expression is consistent with an emerging role for TGF-β1 in regulating expression of genes involved in FAO (Kang et al., 2015). In that regard, our *in vitro* model of EndoMT was associated with a decrease in proliferator-activated receptor (PPAR)-dependent signaling pathways which in turn, appears to regulate CPT1A expression (Figures S1I–S1N). The fall in CPT1A expression appears to have functional consequences. For instance, untreated endothelial cells could respond to an exogenous palmitate challenge with an increase in their oxygen consumption rate (OCR). In contrast, following induction of EndoMT, or after treatment with the CPT1 inhibitor etomoxir, this metabolic response to fatty acids was absent (Figure 1E). Moreover, a direct assessment of palmitate oxidation revealed a marked decline in endothelial FAO following TGF-β stimulation (Figure 1F).

FAO Modulates *In Vitro* EndoMT

To better understand the importance of this EndoMT-induced decline in FAO, we expressed CPT1A using a heterologous promoter in endothelial cells. Surprisingly, constitutive CPT1A expression inhibited the induction of EndoMT mesenchymal markers following TGF-β1/IL-1β treatment, as well as inhibiting the cytokine-induced decline in oxygen consumption (Figures 2A, 2B, and S2A). We next used small hairpin RNAs (shRNAs) to stably knock down CPT1A (CPT1A[KD]; Figures S2B and S2C). In the absence of exogenous cytokines, endothelial cells with reduced CPT1A expression exhibited a more fibroblast-like morphology (Figure 2C). Moreover, these cells activated the EndoMT program (Figures 2D–2G, S2D, and S2E). Similar results were obtained using another shRNA directed against CPT1A (Figure S2F) or using shRNAs directed against CPT2, a

protein that is also required for FAO (Figures S2G and S2H). In addition, while endothelial cells from different vascular beds are known to exhibit markedly different functional characteristics (Nolan et al., 2013), we found that aortic and umbilical vein derived endothelial cells behaved similarly to HPMVECs after FAO inhibition (Figure S2I).

Acetyl-CoA Levels Modulate EndoMT

While CPT1A[KD] endothelial cells exhibited the signature of EndoMT in the absence of any exogenous cytokine stimulation, it is important to note that most cells in culture secrete TGF-β and can respond in an autocrine fashion. In this context, we found that reducing CPT1A expression increased phosphorylation of the TGF-β downstream effector SMAD2, suggesting that inhibiting FAO acted to augment endogenous TGF-β signaling (Figure 3A). Moreover, addition of SB431542, a small molecule inhibitor of TGF-β signaling (Laping et al., 2002), abrogated FAO-dependent SMAD2 activation, as well as the ability of CPT1A inhibition to activate the EndoMT program (Figures 3A, S3A, and S3B).

We next asked how a decrease in endothelial FAO could potentiate TGF-β signaling and thereby modulate the threshold for EndoMT. We thought it possible that stress signaling initiated by altered energetics might play a role; however, we saw no evidence that AMP-activated protein kinase (AMPK) was activated or that there were appreciable alterations in malonyl-CoA levels (Figures S3C–S3E). To further pursue this question, we took note of the increasing evidence suggesting that altering acetyl-CoA levels has broad effects on growth, gene expression, protein function, and cell fate (Cai et al., 2011; Lee et al., 2014; Wellen et al., 2009). Moreover, FAO has, in some cases, been shown to be necessary to maintain cellular acetyl-CoA levels (Pougovkina et al., 2014). Consistent with this, cytokine induction of EndoMT resulted in a fall in acetyl-CoA levels (Figure 3B). To further assess whether this fall in acetyl-CoA levels acts as a trigger for EndoMT, we took advantage of recent observations that supplementing the culture media with acetate can directly increase acetyl-CoA levels through the action of acetyl-CoA synthetase (ACSS2) (Figures 3C and S3F) (Balmer et al., 2016; Moussaieff et al., 2015; Schoors et al., 2015; Schug et al., 2015). We reasoned that if a decline in acetyl-CoA was critical, acetate treatment might prevent cells from undergoing EndoMT. Consistent with this notion, we observed that acetate supplementation inhibited cytokine-stimulated SMAD2 activation (Figure 3D). Acetate treatment also effectively inhibited the EndoMT program (Figures 3E and 3F).

We next asked whether a reciprocal reduction in acetyl-CoA levels could stimulate EndoMT. To lower acetyl-CoA levels, we first took advantage of a specific pharmacological inhibitor of ATP citrate lyase (ACLY), the enzyme that generates acetyl-CoA from citrate (Figure 3C) (Hatzivassiliou et al., 2005). Interestingly, treatment of primary human endothelial cells with the ACLY chemical inhibitor SB-204990 acted as a strong inducer of EndoMT (Figure 3G). A similar effect was obtained by stable knockdown of ACLY (Figures S3G–S3I) or by inhibiting the mitochondrial citrate transporter (CTP; Figure S3J). Besides its direct effect of acetyl-CoA levels, ACLY also modulates *de novo* fatty acid synthesis (Hatzivassiliou et al., 2005).
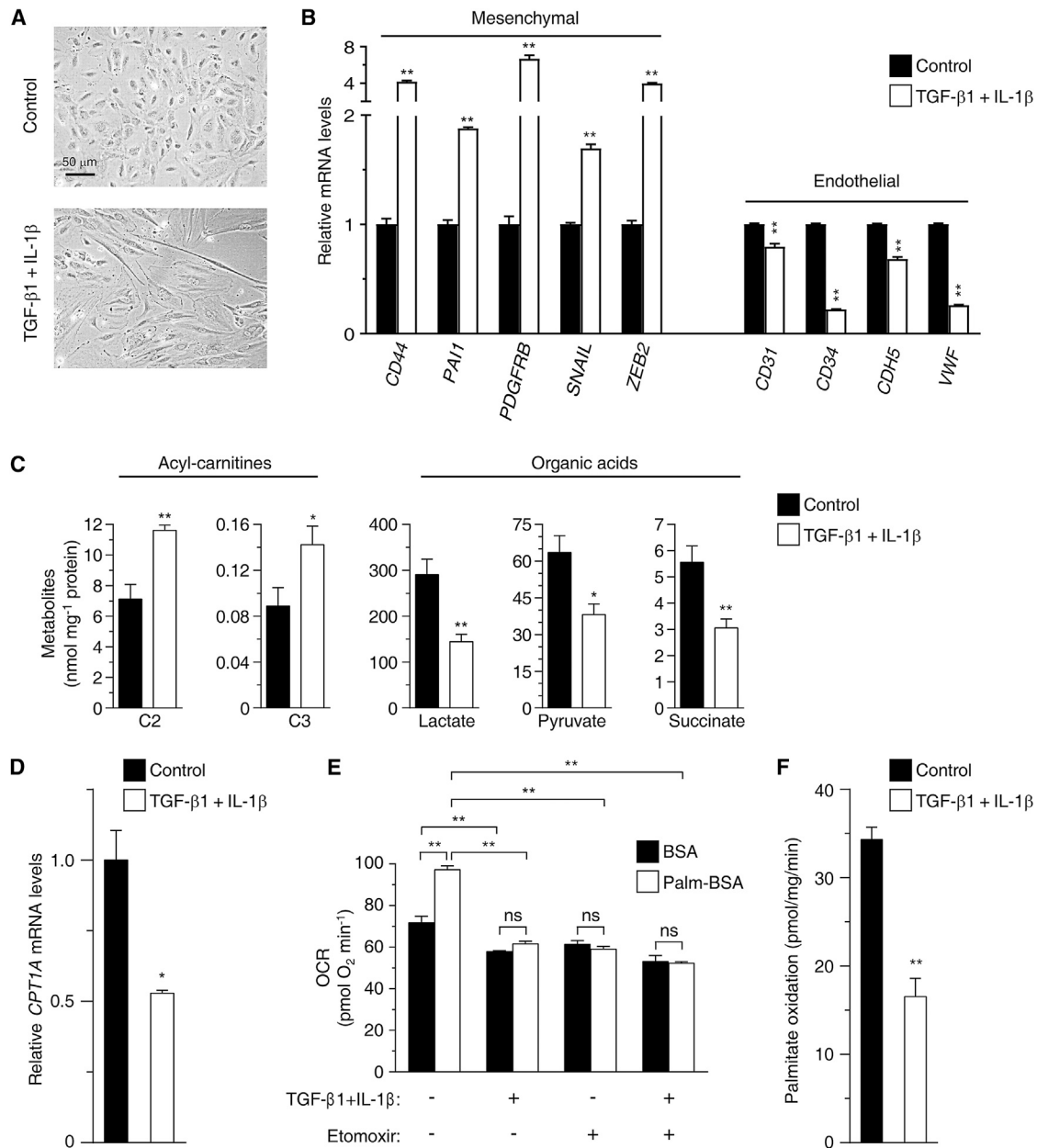
Figure 1. Induction of EndoMT Is Accompanied by an Inhibition of FAO

(A) TGF-β1 and IL-1β induce morphological changes consistent with EndoMT.

(B) Cytokine treatment induces EndoMT (technical triplicates per condition; data represent one of three similar, independent experiments).

(C) Cytokine stimulation reciprocally alters short chain acylcarnitines and the organic acid profile (n = 5 replicates per condition).

(D) Level of endothelial *CPT1A* mRNA expression after cytokine treatment (n = 3 independent experiments).

(E) Cytokine and/or etomoxir treatment suppresses FAO as measured by the inability of palmitate conjugated bovine serum albumin (Palm-BSA) to stimulate the oxygen consumption rate (OCR) (n ≥ 4 technical replicates per condition; data are from one representative experiment of three similar independent experiments).

(F) Rate of FAO after cytokine treatment, using [^{14}C]-labeled palmitate (n = 3 independent experiments).

Data represent mean ± SEM, with significance determined by one-way ANOVA with a Bonferroni's multiple comparison test (E). *$p < 0.05$; **$p < 0.01$; ns, not significant.

However, we saw no induction of EndoMT following stable knockdown of fatty acid synthase (FASN), suggesting that a decrease in fatty acid synthesis is unlikely to be sufficient to mediate cell-fate changes (Figures S3K and S3L). Together, these results suggest that increasing acetyl-CoA levels via acetate supplementation suppresses TGF-β-induced EndoMT, while reducing acetyl-CoA levels via ACLY or CTP inhibition activates EndoMT.

A

TGF-β1 + IL-1β: −   −   +   +
CPT1A: −   +   −   +

WB:

CD44

PAI1

SNAIL

ZEB2

GAPDH

CPT1A

HSP60

B

■ Control
□ Control + CPT1A
■ TGF-β1 + IL-1β
■ TGF-β1 + IL-1β + CPT1A

Relative mRNA levels

CD44   PAI1   SNAIL   ZEB2

C

Control

CPT1A^KD

50 μm

D

Mesenchymal

■ Control
□ CPT1A^KD

Relative mRNA levels

CD44   PAI1   PDGFRB   SNAIL   ZEB2

Endothelial

CD31   CD34   CDH5   VWF

E

Control   CPT1A^KD

PAI1/DAPI

50 μm

F

Control   CPT1A^KD

CD31/DAPI

50 μm

G

PAI1   CD31

■ Control
□ CPT1A^KD

Relative AFI

(legend on next page)

Acetyl-CoA Levels Modulate SMAD7 Inhibitory Signaling

In an attempt to better understand how acetyl-CoA levels might regulate EndoMT, we took advantage of previous observations that SMAD7 acts as a potent inhibitor of TGF-β signaling (Miyazawa and Miyazono, 2017) and that the post-translational acetylation of SMAD7 on two lysine residues (K64 and K70) has been demonstrated to increase SMAD7 protein stability (Grönroos et al., 2002). We therefore reasoned that acetyl-CoA and hence FAO might modulate the strength of TGF-β-associated signaling by regulating the acetylation, and, hence, the post-translational stability of SMAD7. Consistent with this notion, we found that, in endothelial cells, increasing or decreasing acetyl-CoA levels by treating with acetate or an ACLY inhibitor resulted in a corresponding increase or decrease in endogenous SMAD7 protein expression (Figure S3M). In accordance with a post-translational mechanism, we observed that acetate treatment increased SMAD7 acetylation and overall protein levels, without altering *SMAD7* message levels (Figures S3N and S3O). While the effects of acetyl-CoA manipulation on SMAD7 protein levels were seen with wild-type SMAD7 protein (Figure 3H), these same metabolic manipulations did not affect a SMAD7 construct lacking the two known lysine residues that are the targets for acetylation sites (Figure 3I). Similarly, the ability of acetyl-CoA to modulate downstream SMAD2 signaling appeared to require SMAD7 acetylation (Figures S3P and S3Q). Based on these results, we propose a model in which TGF-β signaling results in a positive feedback loop catalyzed by a fall in FAO, a subsequent decline in acetyl-CoA levels and a reduction in SMAD7 inhibition. Our data suggest this enhancement in TGF-β signaling is necessary to drive endothelial cell-fate changes and thus serve as metabolic underpinning for EndoMT susceptibility (Figure S3R).

Acetyl-CoA Levels Modulate SMAD2 Signaling in *Cpt2*-Deficient Mouse Endothelial Cells

To further pursue the physiological implications of these observations, we bred the previously described floxed *Cpt2* mice with transgenic VE-cadherin Cre[+] mice (Alva et al., 2006; Lee et al., 2015) to generate endothelial-specific *Cpt2* knockout (*Cpt2*[E-KO]) mice (Figures S4A and S4B). As expected, expression of CPT2 was markedly reduced in endothelial cells isolated from *Cpt2*[E-KO] animals (Figures 4A and S4C). Moreover, although wild-type (WT) endothelial cells could readily metabolize a fatty acid substrate (palmitate) as evidenced by a marked increase in OCR, this metabolic response was absent in endothelial cells derived from *Cpt2*[E-KO] mice (Figure 4B). The inability to metabolize LCFA did not, however, affect the apparent growth rate of

CPT2-deficient endothelial cells (Figure S4D). This may reflect previous observations that under resting conditions, endothelial cells mostly rely on glycolysis for their energetic needs (De Bock et al., 2013). In addition, as we had observed following CPT1A silencing (Figure 3A), CPT2-knockout endothelial cells also had a constitutive increase in TGF-β-associated SMAD signaling that was inhibited by SB431542 treatment (Figure S4E). Moreover, as we noted following TGF-β stimulation, CPT2-knockout endothelial cells had reduced acetyl CoA levels (Figure 4C). Moreover, acetate treatment could restore acetyl-CoA levels in CPT2-knockout endothelial cells (Figure 4C) and could correspondingly inhibit SMAD2 activation in these cells (Figure 4D).

FAO Modulates *In Vivo* EndoMT

We next asked whether endothelial FAO modulates EndoMT in an *in vivo* context. During development, endocardial cells activated by TGF-β and other ligands are stimulated to undergo EndoMT, triggering their migration into the endocardial cushion and eventual forming the heart valve mesenchyme (Eisenberg and Markwald, 1995; von Gise and Pu, 2012). This process is particularly important for formation of the atrioventricular valves (mitral and tricuspid), while the semilunar valves (aortic and pulmonary) rely less on EndoMT and more on cells derived from the neural crest and the second heart field (von Gise and Pu, 2012). Consistent with a role for FAO in modulating the threshold for EndoMT, morphometric analysis of the mitral valve of *Cpt2*[E-KO] mice demonstrated that endothelial *Cpt2* deletion resulted in marked thickening of the mitral valve (Figures 4E and 4F). Analysis of the aortic valves of *Cpt2*[E-KO] mice revealed a more modest effect of *Cpt2* deletion, consistent with the increased importance of EndoMT in atrioventricular valve formation (Figures S4F and S4G). To further establish that the mitral valve thickening was a consequence of increased EndoMT, we performed lineage tracing analysis using a double-fluorescent reporter mouse (*R26-mTmG*) (Muzumdar et al., 2007). Consistent with previous reports (Alva et al., 2006), *Cpt2*[E-WT];*mTmG* mouse embryos exhibited GFP-positive endothelial cells lining the outer surface of the valve, as well as GFP-positive cells located in the valve interior (Figure 4G). The latter cell type is consistent with cells that have undergone EndoMT during development. Subsequent quantification revealed a significant increase in GFP-positive interstitial cells in *Cpt2*-deficient mouse embryos, consistent with a role for endothelial FAO in restraining the magnitude of physiological EndoMT during embryogenesis (Figure 4H). These differences persisted in adult Cpt2-deficient mice (Figures S4H–S4J).

Figure 2. FAO Modulates *In Vitro* EndoMT

(A) Western blot (WB) analysis demonstrating that heterologous expression of CPT1A inhibits cytokine-induced EndoMT markers.

(B) qRT-PCR analysis of EndoMT markers with or without cytokine treatment, and with or without heterologous CPT1A expression (technical triplicates per condition; data represent one of two independent experiments).

(C) Endothelial cell morphology following knockdown of CPT1A (CPT1A[KD]).

(D) Knockdown of CPT1A activates EndoMT (technical triplicates per condition; results are representative of one of three independent experiments).

(E and F) Representative immunostaining of EndoMT markers in CPT1A[KD] endothelial cells: mesenchymal marker PAI1 (E) or endothelial marker CD31 (F). Nuclei are stained with DAPI.

(G) Quantification of average fluorescence intensity (AFI) of the indicated proteins following knockdown of CPT1A.

Data represent mean ± SEM, with significance determined by one-way ANOVA with a Bonferroni's multiple comparison test (B). *p < 0.05; **p < 0.01; ns, not significant.
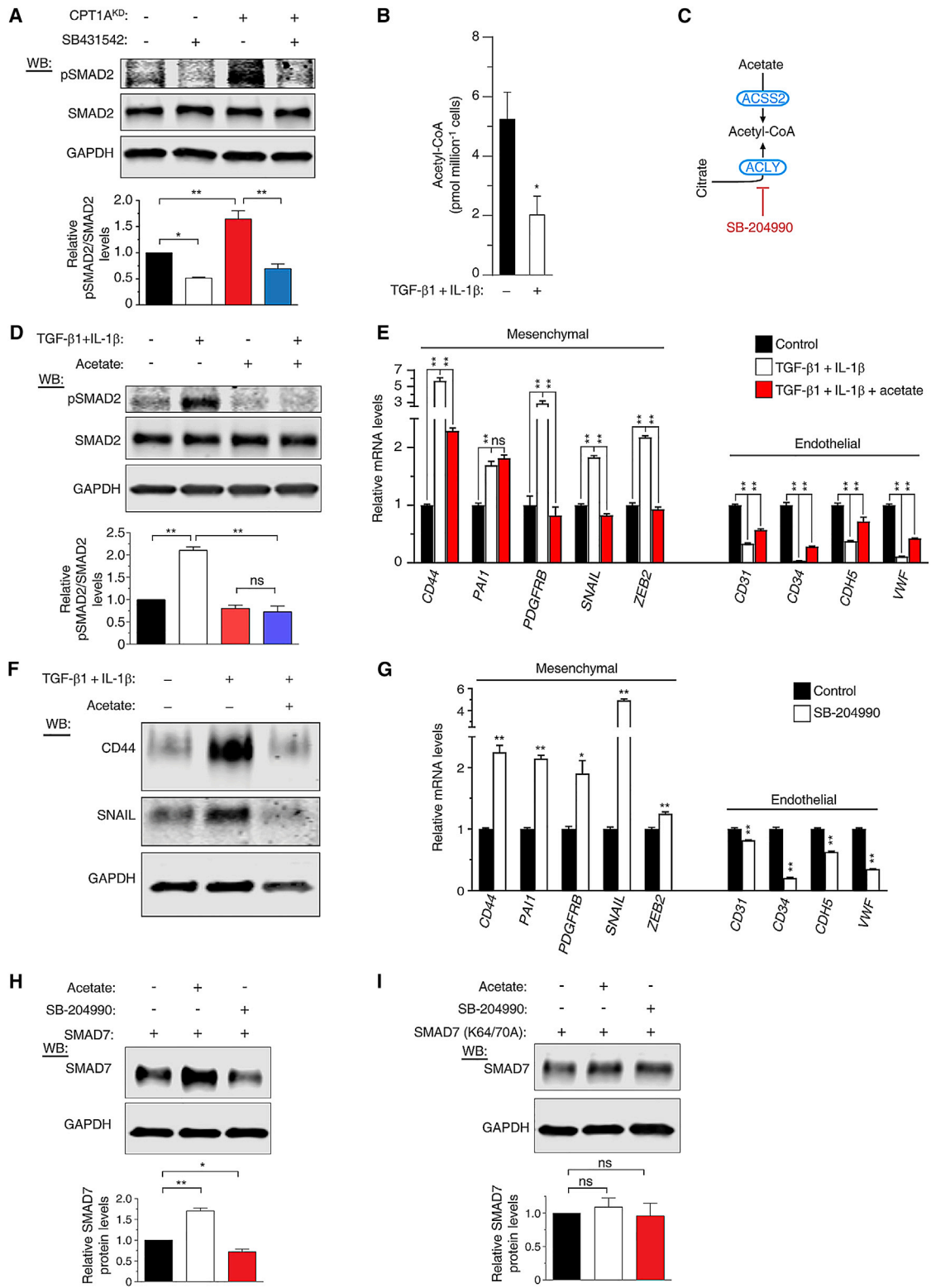
Figure 3. Acetyl-CoA Levels Modulate EndoMT

(A) Representative western blot and quantification of phosphorylated SMAD2 (pSMAD2) in the presence or absence of the TGF-β signaling inhibitor SB431542 following control or CPT1A knockdown (n = 3 independent experiments).

(B) Levels of acetyl-CoA in control or cytokine-treated endothelial cells (n = 3 independent experiments).

(legend continued on next page)

We next sought to ascertain whether endothelial FAO might play a role in restraining EndoMT in the adult animals. We first sought evidence of spontaneous EndoMT using our dual fluorescent reporter to identify vascular endothelial cells (GFP-positive) that simultaneously stained positive for the mesenchymal marker vimentin. Compared to control animals, we observed increased co-localization of GFP and vimentin in the endothelial cells of *Cpt2*^{E-KO} mice (Figures 4I and 4J). To begin to physiologically assess the functional consequences of such changes, we took advantage of previous observations that, following EndoMT, endothelial cells can lose their junctional properties and therefore have impaired barrier function (Good et al., 2015). Consistent with this concept, our analysis using Evans Blue infusions revealed a significant increase in vascular permeability in the kidney, spleen, and lung of the *Cpt2*^{E-KO} mice (Figure 4K).

DISCUSSION

There is increasing evidence that EndoMT might contribute to a wide range of pathological conditions including atherosclerosis, pulmonary hypertension, cardiac valve disease, and organ fibrosis (Kovacic et al., 2012; Sanchez-Duffhues et al., 2016; Yang et al., 2017). The link to fibrosis is particularly intriguing since a previous report has established that kidney fibrosis and subsequent chronic kidney disease (CKD) in both mouse models and human patients is associated with a decrease in FAO (Kang et al., 2015). Indeed, there is considerable evidence that EndoMT participates in the fibrosis associated with CKD (Cruz-Solbes and Youker, 2017; Lovisa et al., 2016). In that regard, based on our observations, we have performed a preliminary genetic analysis of SNPs in both CPT1A and CPT2 and their association with this condition. This initial effort suggests a potential association between FAO and CKD development in humans that may merit further evaluation (Figures S4K and S4L; Table S1).

Our data suggest that decreasing FAO results in a marked decline in basal acetyl-CoA. This defect could be rescued by exogenous acetate supplementation (Figure 4C). These observations are broadly consistent with a previous report that demonstrated that disruption of FAO in endothelial cells inhibited nucleotide synthesis, and that this defect could also be rescued by exogenous acetate supplementation (Schoors et al., 2015). At present, it remains unclear why, in the setting of disrupted FAO, the pool of endothelial acetyl-CoA cannot be maintained by increased utilization of other substrates. Nonetheless, our observations suggest that a fall in acetyl-CoA is a critical modulator of endothelial cell fate. This fall is presumably an early and transient effect, as CPT1A levels largely return to baseline levels 6 days after TGF-β stimulation (Figure S1C). The mechanism behind this restoration of CPT1A expression is currently unclear and will be the subject of future investigations. Finally, although our data suggest that TGF-β signaling, FAO, and EndoMT are linked through the regulation of SMAD7 protein stability (Figure S3R), we cannot exclude that a fall in acetyl-CoA might have additional epigenetic effects that might also contribute to EndoMT susceptibility.

In summary, we demonstrate that endothelial fatty acid metabolism is required to maintain cell fate both *in vitro* and *in vivo*. These observations are broadly consistent with other recent reports where, for instance, the generation of specific T cell and macrophage subtypes has been linked to alterations in substrate utilization (Lochner et al., 2015; Loftus and Finlay, 2016; Norata et al., 2015). Fortunately, a number of pharmacological approaches to increase FAO already exist, including the use of PPAR agonists or FASN inhibitors (Djouadi et al., 2005; Thupari et al., 2004). Given the increasing number of pathological conditions associated with EndoMT, the link between this process and endothelial metabolism could potentially provide important new therapeutic approaches for a wide range of diseases.

STAR★METHODS

Detailed methods are provided in the online version of this paper and include the following:

- KEY RESOURCES TABLE
- CONTACT FOR REAGENT AND RESSOURCES SHARING
- EXPERIMENTAL MODEL AND SUBJECT DETAILS
  - Animals
  - Cells
- METHOD DETAILS
  - Chemicals and reagents
  - Plasmids and lentiviral vectors
  - Western blot and immunoprecipitation analyses
  - Immunostaining
  - Real-time qPCR
  - Metabolic assays
  - Palmitate oxidation rate assay
  - Cardiac valve analysis
  - Cell growth assay
  - High-performance liquid chromatography (HPLC) analysis of malonyl-CoA
  - Determination of endothelial permeability
  - Analysis of genetic variants
- QUANTIFICATION AND STATISTICAL ANALYSIS
- DATA AND SOFTWARE AVAILABILITY

(C) Cytosolic acetyl-CoA levels can be increased by ACSS2-mediated acetate conversion or reduced by the ACLY chemical inhibitor SB-204990. ACLY, ATP citrate lyase; ACSS2, acyl-coenzyme A synthetase short-chain family member 2.

(D) Acetate treatment inhibits cytokine-induced pSMAD2 (n = 3 independent experiments).

(E) Acetate treatment inhibits EndoMT (technical triplicates per condition; data are representative of one of three independent experiments).

(F) Acetate treatment inhibits cytokine-induced EndoMT protein expression.

(G) SB-204990 induces EndoMT (technical triplicates per condition; data represent one of three independent experiments).

(H and I) Western blot analysis of WT SMAD7 protein levels with or without acetate or SB204990 (H) or expression of the K64/70A acetylation-defective SMAD7 mutant under these same conditions (I) (n = 3 independent experiments).

Data represent mean ± SEM, with significance determined by one-way ANOVA with Bonferroni's multiple comparison test (A, D, E, H, and I). *p < 0.05; **p < 0.01; ns, not significant.
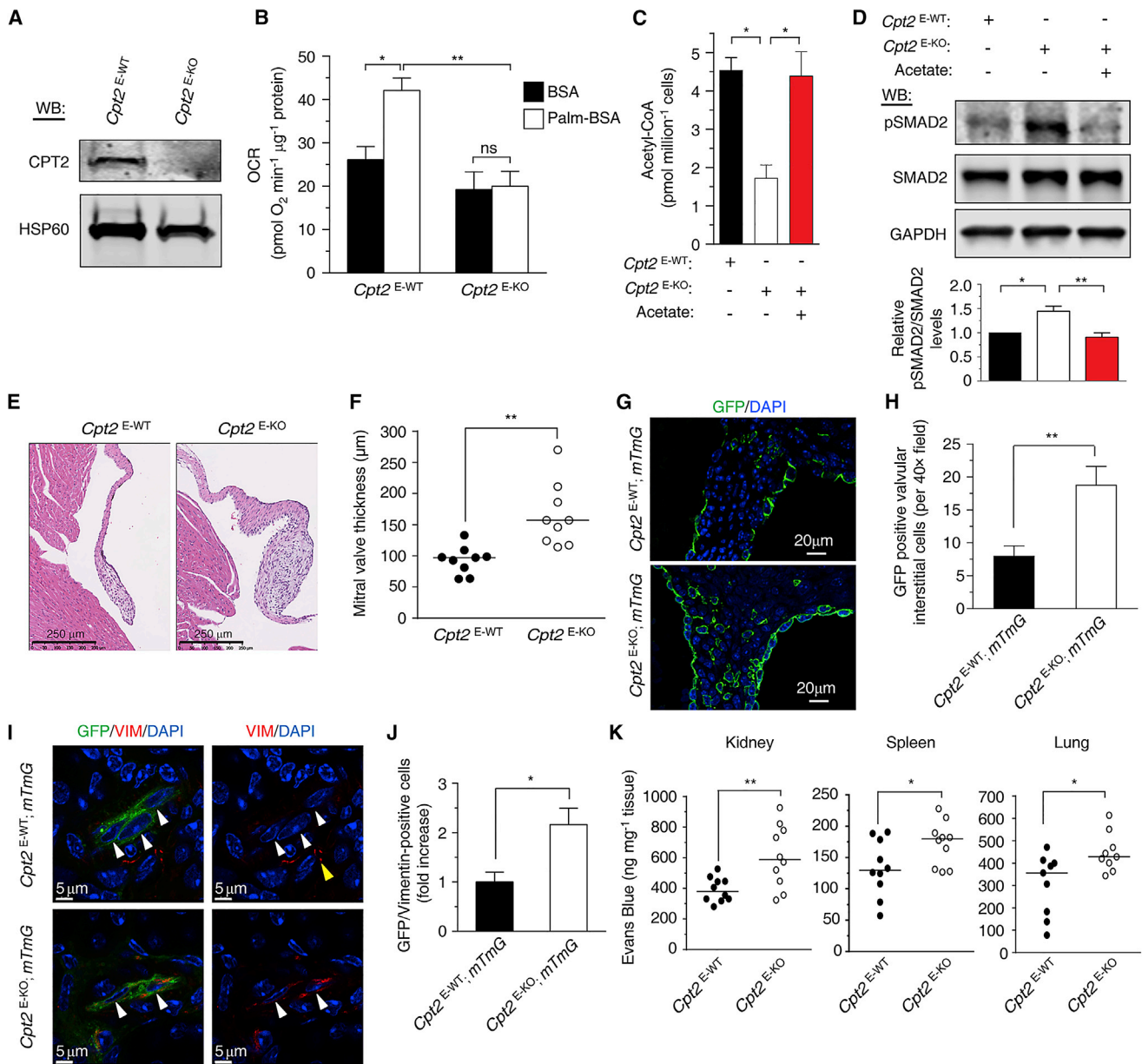
Figure 4. FAO Modulates *In Vivo* EndoMT

(A) Western blot analysis of CPT2 expression in primary lung endothelial cells derived from *Cpt2*[E-WT] or *Cpt2*[E-KO] mice.

(B) Basal OCR of indicated endothelial cells in the presence of BSA alone or Palm-BSA (n = 4 technical replicates per condition; data represent one of three independent experiments).

(C) Level of acetyl-CoA in indicated endothelial cells with or without acetate supplementation (n = 3 independent experiments).

(D) Representative western blot and quantification of pSMAD2 levels with or without acetate treatment as indicated (n = 3 independent experiments).

(E and F) Representative images (E) and quantification (F) of the thickness of the anterior mitral valve leaflet in *Cpt2*[E-WT] and *Cpt2*[E-KO] mice (n = 9 mice per genotype).

(G and H) Representative images (G) and quantification (H) of EndoMT using lineage tracing within the anterior mitral valve leaflet in embryos at approximately E17.5 (n = 5 mouse embryos per genotype).

(I) Representative images from renal parenchyma identifying lineage-traced GFP-positive endothelial cells (white arrows). DAPI was used to stain nuclei. Yellow arrow indicates normal vimentin staining expressed in a non-endothelial cell.

(J) Quantification of renal endothelial cells with histological evidence of EndoMT. Values were normalized to the GFP/vimentin co-localization levels observed in control animals (n = 5 mice per genotype).

(legend continued on next page)

AUTHOR CONTRIBUTIONS

J.X. designed, performed, and analyzed the experiments and aided in writing the manuscript. H.K., Y.Y., J.L., M.M.F., I.I.R., Z.-X.Y., L.R.E., and M.J.J. contributed to the completion of various experiments, Q.S.W., E.L.B., and J.P.F. performed the patient analysis, M.J.W. provided help with the mouse model, and T.F. conceived the study, supervised the research, and contributed to writing the manuscript.

DECLARATION OF INTERESTS

The authors declare no competing interests.

REFERENCES

Alva, J.A., Zovein, A.C., Monvoisin, A., Murphy, T., Salazar, A., Harvey, N.L., Carmeliet, P., and Iruela-Arispe, M.L. (2006). VE-cadherin-Cre-recombinase transgenic mouse: A tool for lineage analysis and gene deletion in endothelial cells. Dev. Dyn. 235, 759–767.

Balmer, M.L., Ma, E.H., Bantug, G.R., Grählert, J., Pfister, S., Glatter, T., Jauch, A., Dimeloe, S., Slack, E., Dehio, P., et al. (2016). Memory CD8(+) t cells require increased concentrations of acetate induced by stress for optimal function. Immunity 44, 1312–1324.

Bonnefont, J.P., Djouadi, F., Prip-Buus, C., Gobin, S., Munnich, A., and Bastin, J. (2004). Carnitine palmitoyltransferases 1 and 2: Biochemical, molecular and medical aspects. Mol. Aspects Med. 25, 495–520.

Cai, L., Sutter, B.M., Li, B., and Tu, B.P. (2011). Acetyl-CoA induces cell growth and proliferation by promoting the acetylation of histones at growth genes. Mol. Cell 42, 426–437.

Chen, P.Y., Qin, L., Baeyens, N., Li, G., Afolabi, T., Budatha, M., Tellides, G., Schwartz, M.A., and Simons, M. (2015). Endothelial-to-mesenchymal transition drives atherosclerosis progression. J. Clin. Invest. 125, 4514–4528.

Cooley, B.C., Nevado, J., Mellad, J., Yang, D., Hilaire, C.S., Negro, A., Fang, F., Chen, G., San, H., Walts, A.D., et al. (2014). TGF-β signaling mediates endothelial-to-mesenchymal transition (EndMT) during vein graft remodeling. Sci. Transl. Med. 6, 227ra34.

Cruz-Solbes, A.S., and Youker, K. (2017). Epithelial to mesenchymal transition (EMT) and endothelial to mesenchymal transition (EndMT): Role and implications in kidney fibrosis. Results Probl. Cell Differ. 60, 345–372.

De Bock, K., Georgiadou, M., Schoors, S., Kuchnio, A., Wong, B.W., Cantelmo, A.R., Quaegebeur, A., Ghesquière, B., Cauwenberghs, S., Eelen,

G., et al. (2013). Role of PFKFB3-driven glycolysis in vessel sprouting. Cell 154, 651–663.

Djouadi, F., Aubey, F., Schlemmer, D., Ruiter, J.P., Wanders, R.J., Strauss, A.W., and Bastin, J. (2005). Bezafibrate increases very-long-chain acyl-CoA dehydrogenase protein and mRNA expression in deficient fibroblasts and is a potential therapy for fatty acid oxidation disorders. Hum. Mol. Genet. 14, 2695–2703.

Eisenberg, L.M., and Markwald, R.R. (1995). Molecular regulation of atrioventricular valvuloseptal morphogenesis. Circ. Res. 77, 1–6.

Evrard, S.M., Lecce, L., Michelis, K.C., Nomura-Kitabayashi, A., Pandey, G., Purushothaman, K.R., d'Escamard, V., Li, J.R., Hadri, L., Fujitani, K., et al. (2016). Endothelial to mesenchymal transition is common in atherosclerotic lesions and is associated with plaque instability. Nat. Commun. 7, 11853.

Good, R.B., Gilbane, A.J., Trinder, S.L., Denton, C.P., Coghlan, G., Abraham, D.J., and Holmes, A.M. (2015). Endothelial to mesenchymal transition contributes to endothelial dysfunction in pulmonary arterial hypertension. Am. J. Pathol. 185, 1850–1858.

Grönroos, E., Hellman, U., Heldin, C.H., and Ericsson, J. (2002). Control of Smad7 stability by competition between acetylation and ubiquitination. Mol. Cell 10, 483–493.

Hatzivassiliou, G., Zhao, F., Bauer, D.E., Andreadis, C., Shaw, A.N., Dhanak, D., Hingorani, S.R., Tuveson, D.A., and Thompson, C.B. (2005). ATP citrate lyase inhibition can suppress tumor cell growth. Cancer Cell 8, 311–321.

Houten, S.M., Violante, S., Ventura, F.V., and Wanders, R.J. (2016). The biochemistry and physiology of mitochondrial fatty acid β-oxidation and its genetic disorders. Annu. Rev. Physiol. 78, 23–44.

Huynh, F.K., Green, M.F., Koves, T.R., and Hirschey, M.D. (2014). Measurement of fatty acid oxidation rates in animal tissues and cell lines. Methods Enzymol. 542, 391–405.

Kang, H.M., Ahn, S.H., Choi, P., Ko, Y.A., Han, S.H., Chinga, F., Park, A.S., Tao, J., Sharma, K., Pullman, J., et al. (2015). Defective fatty acid oxidation in renal tubular epithelial cells has a key role in kidney fibrosis development. Nat. Med. 21, 37–46.

Kovacic, J.C., Mercader, N., Torres, M., Boehm, M., and Fuster, V. (2012). Epithelial-to-mesenchymal and endothelial-to-mesenchymal transition: From cardiovascular development to disease. Circulation 125, 1795–1808.

Laping, N.J., Grygielko, E., Mathur, A., Butter, S., Bomberger, J., Tweed, C., Martin, W., Fornwald, J., Lehr, R., Harling, J., et al. (2002). Inhibition of transforming growth factor (TGF)-beta1-induced extracellular matrix with a novel inhibitor of the TGF-beta type I receptor kinase activity: SB-431542. Mol. Pharmacol. 62, 58–64.

Lee, J.V., Carrer, A., Shah, S., Snyder, N.W., Wei, S., Venneti, S., Worth, A.J., Yuan, Z.F., Lim, H.W., Liu, S., et al. (2014). Akt-dependent metabolic reprogramming regulates tumor cell histone acetylation. Cell Metab. 20, 306–319.

Lee, J., Ellis, J.M., and Wolfgang, M.J. (2015). Adipose fatty acid oxidation is required for thermogenesis and potentiates oxidative stress-induced inflammation. Cell Rep. 10, 266–279.

Lochner, M., Berod, L., and Sparwasser, T. (2015). Fatty acid metabolism in the regulation of T cell function. Trends Immunol. 36, 81–91.

Loftus, R.M., and Finlay, D.K. (2016). Immunometabolism: Cellular metabolism turns immune regulator. J. Biol. Chem. 291, 1–10.

Lovisa, S., Zeisberg, M., and Kalluri, R. (2016). Partial epithelial-to-mesenchymal transition and other new mechanisms of kidney fibrosis. Trends Endocrinol. Metab. 27, 681–695.

Magrini, E., Villa, A., Angiolini, F., Doni, A., Mazzarol, G., Rudini, N., Maddaluno, L., Komuta, M., Topal, B., Prenen, H., et al. (2014). Endothelial

(K) Quantification of Evans Blue dye extravasation into the parenchyma of the kidney (n = 10 mice per genotype), spleen (n = 10 mice per genotype), and lung (n = 9 mice per genotype) of $Cpt2^{E-WT}$ and $Cpt2^{E-KO}$ mice.

Data represent scatterplots with the median value indicated (F, K). Data represent mean ± SEM, with significance determined by one-way ANOVA with Bonferroni's multiple comparison test (B–D). *$p < 0.05$; **$p < 0.01$; ns, not significant.

deficiency of L1 reduces tumor angiogenesis and promotes vessel normalization. J. Clin. Invest. *124*, 4335–4350.

Miyazawa, K., and Miyazono, K. (2017). Regulation of TGF-β family signaling by inhibitory Smads. Cold Spring Harb. Perspect. Biol. *9*. Published online March 1, 2017. https://doi.org/10.1101/cshperspect.a022095.

Moussaieff, A., Rouleau, M., Kitsberg, D., Cohen, M., Levy, G., Barasch, D., Nemirovski, A., Shen-Orr, S., Laevsky, I., Amit, M., et al. (2015). Glycolysis-mediated changes in acetyl-CoA and histone acetylation control the early differentiation of embryonic stem cells. Cell Metab. *21*, 392–402.

Muzumdar, M.D., Tasic, B., Miyamichi, K., Li, L., and Luo, L. (2007). A global double-fluorescent Cre reporter mouse. Genesis *45*, 593–605.

Nolan, D.J., Ginsberg, M., Israely, E., Palikuqi, B., Poulos, M.G., James, D., Ding, B.S., Schachterle, W., Liu, Y., Rosenwaks, Z., et al. (2013). Molecular signatures of tissue-specific microvascular endothelial cell heterogeneity in organ maintenance and regeneration. Dev. Cell *26*, 204–219.

Norata, G.D., Caligiuri, G., Chavakis, T., Matarese, G., Netea, M.G., Nicoletti, A., O'Neill, L.A., and Marelli-Berg, F.M. (2015). The cellular and molecular basis of translational immunometabolism. Immunity *43*, 421–434.

Piera-Velazquez, S., Li, Z., and Jimenez, S.A. (2011). Role of endothelial-mesenchymal transition (EndoMT) in the pathogenesis of fibrotic disorders. Am. J. Pathol. *179*, 1074–1080.

Potenta, S., Zeisberg, E., and Kalluri, R. (2008). The role of endothelial-to-mesenchymal transition in cancer progression. Br. J. Cancer *99*, 1375–1379.

Pougovkina, O., te Brinke, H., Ofman, R., van Cruchten, A.G., Kulik, W., Wanders, R.J., Houten, S.M., and de Boer, V.C. (2014). Mitochondrial protein acetylation is driven by acetyl-CoA from fatty acid oxidation. Hum. Mol. Genet. *23*, 3513–3522.

Radu, M., and Chernoff, J. (2013). An in vivo assay to test blood vessel permeability. J. Vis. Exp. Published online March 16, 2013. https://doi.org/10.3791/50062.

Reynolds, L.E., and Hodivala-Dilke, K.M. (2006). Primary mouse endothelial cell culture for assays of angiogenesis. Methods Mol. Med. *120*, 503–509.

Rieder, F., Kessler, S.P., West, G.A., Bhilocha, S., de la Motte, C., Sadler, T.M., Gopalan, B., Stylianou, E., and Fiocchi, C. (2011). Inflammation-induced endothelial-to-mesenchymal transition: A novel mechanism of intestinal fibrosis. Am. J. Pathol. *179*, 2660–2673.

Roden, D.M., Pulley, J.M., Basford, M.A., Bernard, G.R., Clayton, E.W., Balser, J.R., and Masys, D.R. (2008). Development of a large-scale de-identified DNA biobank to enable personalized medicine. Clin. Pharmacol. Ther. *84*, 362–369.

Sanchez-Duffhues, G., Orlova, V., and Ten Dijke, P. (2016). In brief: Endothelial-to-mesenchymal transition. J. Pathol. *238*, 378–380.

Schoors, S., Bruning, U., Missiaen, R., Queiroz, K.C., Borgers, G., Elia, I., Zecchin, A., Cantelmo, A.R., Christen, S., Goveia, J., et al. (2015). Fatty acid carbon is essential for dNTP synthesis in endothelial cells. Nature *520*, 192–197.

Schug, Z.T., Peck, B., Jones, D.T., Zhang, Q., Grosskurth, S., Alam, I.S., Goodwin, L.M., Smethurst, E., Mason, S., Blyth, K., et al. (2015). Acetyl-CoA synthetase 2 promotes acetate utilization and maintains cancer cell growth under metabolic stress. Cancer Cell *27*, 57–71.

Stenmark, K.R., Frid, M., and Perros, F. (2016). Endothelial-to-mesenchymal transition: An evolving paradigm and a promising therapeutic target in PAH. Circulation *133*, 1734–1737.

Thupari, J.N., Kim, E.K., Moran, T.H., Ronnett, G.V., and Kuhajda, F.P. (2004). Chronic C75 treatment of diet-induced obese mice increases fat oxidation and reduces food intake to reduce adipose mass. Am. J. Physiol. Endocrinol. Metab. *287*, E97–E104.

von Gise, A., and Pu, W.T. (2012). Endocardial and epicardial epithelial to mesenchymal transitions in heart development and disease. Circ. Res. *110*, 1628–1645.

Wellen, K.E., Hatzivassiliou, G., Sachdeva, U.M., Bui, T.V., Cross, J.R., and Thompson, C.B. (2009). ATP-citrate lyase links cellular metabolism to histone acetylation. Science *324*, 1076–1080.

Yang, B., Zhou, W., Jiao, J., Nielsen, J.B., Mathis, M.R., Heydarpour, M., Lettre, G., Folkersen, L., Prakash, S., Schurmann, C., et al. (2017). Protein-altering and regulatory genetic variants near GATA4 implicated in bicuspid aortic valve. Nat. Commun. *8*, 15481.

Zeisberg, E.M., Tarnavski, O., Zeisberg, M., Dorfman, A.L., McMullen, J.R., Gustafsson, E., Chandraker, A., Yuan, X., Pu, W.T., Roberts, A.B., et al. (2007). Endothelial-to-mesenchymal transition contributes to cardiac fibrosis. Nat. Med. *13*, 952–961.

Zeisberg, E.M., Potenta, S.E., Sugimoto, H., Zeisberg, M., and Kalluri, R. (2008). Fibroblasts in kidney fibrosis emerge via endothelial-to-mesenchymal transition. J. Am. Soc. Nephrol. *19*, 2282–2287.

STAR★METHODS

KEY RESOURCES TABLE

REAGENT or RESOURCE	SOURCE	IDENTIFIER
Antibodies		
Alexa Fluor 488 AffiniPure donkey anti-Chicken IgY	Jackson ImmunoResearch Labs	Cat#703-545-155; RRID:AB_2340375
Alexa Fluor 488 goat anti-Rabbit IgG	Thermo Fisher Scientific	Cat#A-11034; RRID: AB_2576217
Alexa Fluor 555 donkey anti-Rabbit IgG	Thermo Fisher Scientific	Cat#A-31572; RRID: AB_162543
Alexa Fluor 647 goat anti-Rabbit IgG	Cell Signaling Technology	Cat#4414; RRID: AB_10693544
Alexa Fluor 647 rat polyclonal anti-mouse CD45	BioLegend	Cat#103124; RRID: AB_493533
APC rat monoclonal anti-mouse CD31	BD Biosciences	Cat#551262; RRID: AB_398497
Chicken polyclonal anti-GFP	Abcam	Cat#ab13970; RRID: AB_300798
Fluorescent TrueBlot: anti-Rabbit IgG DyLight 800	Rockland	Cat#18-4516-32; RRID: AB_2610841
Goat polyclonal anti-HSP60	Santa Cruz Biotechnology	Cat#sc-1052; RRID: AB_631683
Mouse monoclonal anti-AMPKα	Cell Signaling Technology	Cat#2793; RRID: AB_915794
Mouse monoclonal anti-CPT1A	Abcam	Cat#ab128568; RRID: AB_11141632
Mouse monoclonal anti-FLAG M2	Sigma-Aldrich	Cat#F1804; RRID: AB_262044
Rabbit monoclonal anti-ACC	Cell Signaling Technology	Cat#3676; RRID: AB_2219397
Rabbit monoclonal anti-CPT2	Abcam	Cat#ab181114; RRID: AB_2687503
Rabbit monoclonal anti-GAPDH	Cell Signaling Technology	Cat#5174; RRID: AB_10622025
Rabbit monoclonal anti-pAMPKα	Cell Signaling Technology	Cat#2535; RRID: AB_331250
Rabbit monoclonal anti-pSmad1/5/8	Cell Signaling Technology	Cat#13820; RRID: AB_2493181
Rabbit monoclonal anti-pSmad2	Cell Signaling Technology	Cat#3108; RRID: AB_490941
Rabbit monoclonal anti-Smad2	Cell Signaling Technology	Cat#5339; RRID: AB_10626777
Rabbit monoclonal anti-Snail	Cell Signaling Technology	Cat#3879S; RRID: AB_2255011
Rabbit monoclonal anti-Vimentin	Cell Signaling Technology	Cat#5741; RRID:AB_10695459
Rabbit polyclonal anti-acetylated-lysine	Cell Signaling Technology	Cat#9441; RRID: AB_331805
Rabbit polyclonal anti-ACLY	Cell Signaling Technology	Cat#4332; RRID: AB_2223744
Rabbit polyclonal anti-CD31	Abcam	Cat#ab28364; RRID: AB_726362
Rabbit polyclonal anti-CD44	GeneTex	Cat#GTX102111; RRID: AB_1240596
Rabbit polyclonal anti-FASN	Cell Signaling Technology	Cat#3189; RRID: AB_2100798
Rabbit polyclonal anti-pACC	Millipore	Cat# 07-303; RRID:AB_310504
Rabbit polyclonal anti-PAI1	Abcam	Cat#ab66705; RRID: AB_1310540
Rabbit polyclonal anti-Smad1/5/8	Santa Cruz Biotechnology	Cat# sc-6031-R; RRID: AB_785721
Rabbit polyclonal anti-Smad7	GeneTex	Cat#GTX59874; RRID: AB_10731930
Rabbit polyclonal anti-Zeb2	Millipore	Cat#ABE573
Rat monoclonal anti-mouse CD16/CD32	BD Biosciences	Cat#553142; RRID:AB_394657
Rat monoclonal anti-mouse CD102	BD Biosciences	Cat#553326; RRID: AB_394784
Chemicals, Peptides, and Recombinant Proteins		
5-Sulfosalicylic acid dihydrate	Sigma-Aldrich	Cat#S3147-100G
Bovine serum albumin	Sigma-Aldrich	Cat#A7030-10G
Collagenase, Type I, powder	Thermo Fisher Scientific	Cat#17100017
CTP Inhibitor	Sigma-Aldrich	Cat#SML0068-25MG
Endothelial cell growth supplement from bovine neural tissue, suitable for cell culture	Sigma-Aldrich	Cat#E2759-15MG
Etomoxir sodium salt	Bio-Techne	Cat#4539
Evans Blue	J. T. Baker Chemicals	Cat#M372-02
Fibronectin from bovine plasma	Sigma-Aldrich	Cat#F4759-2MG

(Continued on next page)

Continued

REAGENT or RESOURCE	SOURCE	IDENTIFIER
Fibronectin from human plasma	Sigma-Aldrich	Cat#F2006-2MG
Heparin sodium salt from porcine intestinal mucosa	Sigma-Aldrich	Cat#H3393-100KU
Heparin sodium salt, suitable for cell culture	Sigma-Aldrich	Cat#H3149-100KU
IL-1β	Peprotech	Cat#200-01B
L-Carnitine hydrochloride	Sigma-Aldrich	Cat#C0283-5G
Malonyl coenzyme A lithium salt	Sigma-Aldrich	Cat#M4263-10MG
SB-204990	Tocris	Cat#4962
SB431542	Selleck Chemicals	Cat#S1067
Sodium acetate	Sigma-Aldrich	Cat#S5636-500G
Sodium bicarbonate	Sigma-Aldrich	Cat#792519
Sodium butyrate	Sigma-Aldrich	Cat#B5887-1G
Sodium palmitate	Sigma-Aldrich	Cat#P9767
Sodium phosphate monobasic monohydrate	Sigma-Aldrich	Cat#S9638-500G
TGF-β1	Peprotech	Cat#100-21C
Critical Commercial Assays		
Anti-FLAG M2 Magnetic Beads	Sigma-Aldrich	Cat#M8823
Dynabeads Sheep Anti-Rat IgG	Thermo Fisher Scientific	Cat#11035
FastStart Universal SYBR Green Master (Rox)	Roche	Cat#04913914001
iScript cDNA Synthesis Kit	Bio-Rad	Cat#1708891
Mitochondria Isolation Kit for Cultured Cells	Thermo Fisher Scientific	Cat#89874
MTT-based colorimetric kit	Millipore	Cat#CT02
Palmitic acid, [1-14C]-, 50 μCi	PerkinElmer	Cat#NEC075H050UC
PicoProbe acetyl-CoA fluorometric assay kit	BioVision	Cat#K317-100
Pierce BCA protein assay kit	Thermo Fisher Scientific	Cat#23225
PureLink HiPure Plasmid Filter Maxiprep Kit	Thermo Fisher Scientific	Cat#K2100-16
RNase-free DNase Set	QIAGEN	Cat#79254
RNeasy Mini Kit	QIAGEN	Cat#74106
Seahorse XF Palmitate-BSA FAO Substrate	Agilent	Cat#102720-100
ZymoPURE Plasmid Maxiprep Kit	Zymo Research	Cat#D4202
Deposited Data		
N/A		
Experimental Models: Cell Lines		
Human 293T cell line	Clontech	Cat#632180
Human HeLa cell line	ATCC	Cat#ATCC CCL-2
Experimental Models: Organisms/Strains		
Mice with endothelial-specific deletion of *Cpt2*	This paper	N/A
Mice with endothelial-specific deletion of *Cpt2* and Cre reporter mT/mG labeling	This paper	N/A
Oligonucleotides		
Primers for real-time qPCR	Integrated DNA Technologies	Table S2
Recombinant DNA		
Empty control vector for pReceiver-Lv105	GeneCopoeia	Cat#EX-NEG-Lv105
pLVX-Puro-SMAD7	This paper	N/A
pLVX-Puro-SMAD7-K64/70A	This paper	N/A
pReceiver-Lv102-SMAD7, flag-tagged	GeneCopoeia	Cat#EX-Z7607-Lv102
pReceiver-Lv105-CPT1A	GeneCopoeia	Cat#EX-A1436-Lv105
TRC lentiviral scrambled shRNA control	Addgene	Cat#1864
TRC lentiviral human ACLY shRNA	Sigma-Aldrich	Cat#TRCN0000291890

Continued

REAGENT or RESOURCE	SOURCE	IDENTIFIER
TRC lentiviral human CPT1A shRNA	Sigma-Aldrich	Cat#TRCN0000036282; Cat#TRCN0000036283
TRC lentiviral human CPT2 shRNA	Dharmacon	Cat#RHS3979-201735361
TRC lentiviral human FASN shRNA	Sigma-Aldrich	Cat#TRCN0000003128
TRC lentiviral human PPARD shRNA	Dharmacon	Cat#RHS3979-201733936; Cat#RHS3979-201733937
TRC lentiviral human PPARG shRNA	Dharmacon	Cat#RHS3979-201733944; Cat#RHS3979-201733948
Software and Algorithms		
BD FACSDiva software v8.0	BD Biosciences	http://www.bdbiosciences.com/us/instruments/research/software/flow-cytometry-acquisition/bd-facsdiva-software/m/111112/overview
ChemStation Rev. A.10.01	Agilent	https://www.agilent.com/en/products/software-informatics/chromatography-data-systems/chemstation-data-browser-software-module
GraphPad Prism 7.02	GraphPad Software	https://www.graphpad.com/scientific-software/prism/
Huygens	Scientific Volume Imaging	https://svi.nl/HuygensSoftware
Image Studio Lite Ver 5.2	LI-COR Biosciences	https://www.licor.com/bio/products/software/image_studio/
Imaris 9.0.2	BITPLANE	http://www.bitplane.com/
iVision 4.0.13	BioVision Technologies	http://www.biovis.com/ivision.html
MetaMorph Offline 7.8.12.0	Molecular Devices	https://www.moleculardevices.com/systems/metamorph-research-imaging
NDP.view2	Hamamatsu Photonics	http://www.hamamatsu.com/us/en/community/nanozoomer/Software/NDPView.html
Primer-BLAST	NCBI	https://www.ncbi.nlm.nih.gov/tools/primer-blast/
SoftMax Pro 7.0	Molecular Devices	https://www.moleculardevices.com/systems/microplate-readers/softmax-pro-7-software
Wave 2.4.0	Agilent	https://www.agilent.com/en-us/products/cell-analysis-(seahorse)/seahorse-wave-software
ZEN	ZEISS	https://www.zeiss.com/microscopy/us/products/microscope-software/zen.html

CONTACT FOR REAGENT AND RESSOURCES SHARING

Further information and requests for reagents may be directed to, and will be fulfilled by, the Lead Contact, Toren Finkel (finkelt@pitt.edu).

EXPERIMENTAL MODEL AND SUBJECT DETAILS

Animals

Cpt2$^{flox/flox}$ mice have been described previously (Lee et al., 2015) and were crossed with VE-cadherin Cre mice (Jackson Laboratory) (Alva et al., 2006) to generate mice with endothelial-specific deletion of *Cpt2* (*Cpt2*$^{E-KO}$ mice). *Cpt2*$^{E-KO}$ mice were crossed with the global double-fluorescent Cre reporter mice (R26-mT/mG; Jackson Laboratory) (Muzumdar et al., 2007) to generate mice with endothelial-specific deletion of Cpt2 and Cre reporter mT/mG labeling (*Cpt2*$^{E-KO}$; mTmG mice). All mice were on a C57BL/6J background and were genotyped by standard PCR-based methods. Unless stated otherwise, male and female mice were analyzed and each experiment described (e.g., permeability, valve thickness, etc.) used an independent cohort of animals. All experiments were approved by the NHLBI Animal Care and Use Committee of the NIH.

Cells

Mouse endothelial cells were isolated and cultured as previously described (Reynolds and Hodivala-Dilke, 2006). Briefly, after dissection and mincing, three mouse lungs were digested in 10 mL of PBS containing 0.1% type I collagenase (Life Technologies) at 37°C for 1 hour. The suspension was filtered through a cell strainer (Corning), collected by centrifugation, and then plated on fibronectin (Sigma-Aldrich, F4759)-, gelatin (Sigma-Aldrich, G1393)- and collagen (Sigma-Aldrich, C4243)-coated T-75 flasks. Sequential sorting was

carried out using sheep anti-rat IgG Dynabeads (Life Technologies) coated with BD Pharmingen purified rat anti-mouse CD16/CD32 antibody (BD Biosciences, cat. # 553142) to remove macrophages and then BD Pharmingen Purified Rat Anti-Mouse CD102 antibody (Biosciences, Cat#553326) to isolate endothelial cells. Purity was assessed using an allophycocyanin (APC)-conjugated rat anti-mouse CD31 (PECAM1) antibody (BD Biosciences, Cat#551262, 1:70 dilution). Data for purity were acquired and analyzed using a FACSCanto and the BD FACSDiva software v8.0 (BD Biosciences). The freshly isolated mouse endothelial cells were maintained in Dulbecco's Modification of Eagle's Medium (DMEM)/F12 (Life Technologies) supplemented with 20% (v/v) fetal bovine serum (FBS; Life Technologies), 2 mM L-glutamine (Life Technologies), 0.1 mg ml^{-1} heparin (Sigma-Aldrich), 0.05 mg ml^{-1} endothelial cell growth supplement (Sigma-Aldrich), 100 U ml^{-1} penicillin and 100 μg ml^{-1} streptomycin and used between passages 1 and 4. Primary human pulmonary microvascular endothelial cells (HPMVECs), human umbilical vein endothelial cells (HUVECs) and human aortic endothelial cells (HAECs) were obtained from Lonza and grown on fibronectin (Sigma-Aldrich, F2006)-coated cell culture plates. HPMVECs were maintained in EGM-2 MV BulletKit (basal medium and SingleQuots Kit) medium (Lonza) or Endothelial Cell Growth Medium MV2 (PromoCell), while HAECs and HUVECs were maintained in EGM-2 BulletKit (Lonza). The commercially purchased human endothelial cells were used between passages 4 and 9. HeLa (American Type Culture Collection) and 293T (Clontech) cells were cultured in DMEM containing 4.5 g L^{-1} glucose, L-glutamine and sodium pyruvate (Corning) supplemented with 10% (v/v) FBS (Life Technologies), 100 U ml^{-1} penicillin and 100 μg ml^{-1} streptomycin (Life Technologies). Cell morphology was examined using a Nikon Eclipse TE300 inverted microscope (Nikon Instruments) and images were acquired using iVision software (version 4.0.13).

METHOD DETAILS

Chemicals and reagents
For cytokine induction of EndoMT, subconfluent endothelial cells on fibronectin-coated plates were incubated with 10 ng ml^{-1} TGF-β1 (Peprotech) and 1 ng ml^{-1} IL-1β (Peprotech). After 2 days of cytokine treatment, real-time quantitative PCR (qPCR) measurement of *SNAIL* mRNA expression was performed, while mRNA levels for other EndoMT markers (*CD31*, *CD34*, *CD44*, *CDH5*, *PAI1*, *PDGFRB*, *VWF* and *ZEB2*) were assessed 7 days of cytokine treatment. For chemical induction of EndoMT, subconfluent endothelial cells on fibronectin-coated 6-well plates were incubated with the ACLY inhibitor, SB-204990 (Tocris) at final concentration of 60 μM or with a mitochondrial citrate transport protein (CTP) inhibitor (Sigma-Aldrich) at a final concentration of 1 mM. After 0.5 hours of SB-204990 or 3 hours of CTP inhibitor treatment, real-time qPCR measurement of *SNAIL* mRNA expression was performed, while the other mRNA EndoMT markers were assessed 1 day after SB-204990 treatment or 2 days after CTP inhibitor treatment. Sodium acetate (Sigma-Aldrich) was added, where indicated, at a concentration of 40 mM, a concentration similar to what has been previously employed (Schoors et al., 2015). The CPT1 inhibitor, etomoxir (Bio-Techne), was used at a final concentration of 100 μM. The inhibitor of TGFβ signaling, SB431542 (Selleck Chemicals), was added at a final concentration of 10 μM.

Plasmids and lentiviral vectors
The following lentiviral vectors for stable shRNA-mediated knockdown of human gene expression were used: shACLY, shCPT1A, shCPT2, shFASN, shPPARD, shPPARG, and a scrambled shRNA control (shSCR, Addgene, Plasmid #1864). The lentiviral vector for overexpression of human CPT1A (EX-A1436-Lv105) and its vector control (EX-NEG-Lv105) were purchased from GeneCopoeia and validated by DNA sequencing (Eurofins MWG Operon). The lentiviral vectors for overexpression of human SMAD7 (GeneCopoeia, EX-Z7607-Lv102) and its mutant version with K64/70A were cloned in pLVX-Puro vectors (Clontech) and validated by DNA sequencing (Eurofins MWG Operon). Plasmids were purified using ZymoPURE Plasmid Maxiprep Kit (Zymo Research) with VM20 Vacuum Manifold (Sigma-Aldrich) or PureLink HiPure Plasmid Filter Maxiprep Kit (Life Technologies), and their concentration determined using the NanoDrop 2000 spectrophotometer (Thermo Fisher Scientific). Lentiviral supernatants were collected 48 hours after transfection of 293T cells (Clontech), using the Lenti-X concentrator (Clontech), and then aliquoted and stored at −80°C. For lentiviral titration, viral RNA was isolated using a NucleoSpin RNA Virus Kit (Clontech) and the copy number of the viral RNA genome determined using a Lenti-X qRT-PCR (quantitative RT-PCR) Titration Kit (Clontech). Cells were infected (approximately 1-2 × 10^9 copies per million cells) in the presence of Polybrene (Santa Cruz Biotechnology) at final concentration of 8 μg ml^{-1} and incubated with the virus mixture. After overnight incubation, the media was replaced with complete fresh growth media prior to selection with puromycin (Sigma-Aldrich; endothelial cells, 2 μg ml^{-1}; HeLa, 0.5 μg ml^{-1}). For CPT1A-knockdown-mediated induction of EndoMT, human endothelial cells were initially seeded evenly at 7,500-10,000 cells cm^{-2} in 6-well plates. The next day, subconfluent cells were infected with lentiviruses expressing shRNAs against CPT1A or control shRNAs. For analysis of EndoMT markers, cells were assessed 5 days after lentiviral transduction.

Western blot and immunoprecipitation analyses
For analysis of endothelial CPT1A, CPT2 and HSP60 protein levels, mitochondrial proteins were isolated using the Mitochondria Isolation Kit for Cultured Cells (Thermo Fisher Scientific) according to the manufacturer's protocol. For western blot analysis of other proteins, endothelial cells were collected in RIPA Buffer (Boston Bioproducts) supplemented with Protease Inhibitor Cocktail (Roche) and Phosphatase Inhibitor Cocktail (Roche) or Pierce IP Lysis Buffer (25 mM Tris-HCl pH 7.4, 150 mM NaCl, 1% NP-40, 1 mM EDTA and 5% glycerol; Thermo Fisher Scientific) supplemented with Protease Inhibitor Cocktail (Roche), Phosphatase Inhibitor Cocktail (Roche) and 10 mM of histone deacetylase inhibitor sodium butyrate (Sigma-Aldrich). Protein concentration was determined using

a Pierce BCA protein assay kit (Thermo Fisher Scientific). Protein lysates were separated by SDS-PAGE using 4%–20% Mini-PROTEAN TGX Precast Gels (Bio-Rad) and Mini-PROTEAN Tetra Electrophoresis Cell (Bio-Rad), and then transferred to a 0.2 μM nitrocellulose membrane using Trans-Blot Turbo Transfer System (Bio-Rad). Following blocking in Odyssey Blocking Buffer (LI-COR), the membranes were incubated with the indicated primary antibodies. After washing with PBST (PBS + 0.1% Tween-20 (Sigma-Aldrich)) three times, each for 5 minutes, the membranes were incubated with near-infrared fluorescent IRDye secondary antibodies for 1 hour at room temperature. For analysis of SMAD7 acetylation, HeLa cells were infected with lentivirus expressing Flag-tagged human SMAD7 with or without treatment of acetate (72 hours), and then lysed in ice-cold Pierce IP Lysis Buffer (Thermo Fisher Scientific) supplemented with Protease Inhibitor Cocktail (Roche), Phosphatase Inhibitor Cocktail (Roche) and 10 mM of histone deacetylase inhibitor sodium butyrate (Sigma-Aldrich). Immunoprecipitation was carried out by adding Anti-FLAG M2 Magnetic Beads (Sigma-Aldrich, M8823) into the pre-cleared cell lysate, followed by incubation at 4°C overnight. After washing, the immunoprecipitates were resolved by SDS-PAGE and transferred to 0.2 μM nitrocellulose membrane as above. After blocking with 5% bovine serum albumin (BSA; Sigma-Aldrich) in PBS, the membranes were subjected to western blot analysis using a primary rabbit polyclonal antibody to acetylated-lysine residues (Cell Signaling, 9441) followed by a secondary fluorescent TrueBlot Anti-Rabbit IgG DyLight 800 antibody (Rockland Immunochemicals, 18-4516-32). Detection and quantification of target proteins were performed with the ODYSSEY CLx Infrared Imaging System and Image Studio Lite version 5.2 Software (LI-COR). Protein expression was normalized to the corresponding expression of the indicated control protein (GAPDH was used as a loading control for whole-cell extracts; HSP60 was used as a loading control for mitochondrial extracts).

Immunostaining

For immunocytochemical detection of EndoMT, endothelial cells were grown in tissue culture treated glass slides (BD Biosciences, 354104), washed with PBS, and fixed in PBS supplemented with 4% paraformaldehyde (Electron Microscopy Sciences) for 20 minutes at room temperature. After permeabilization with 0.3% Triton X-100 (Sigma-Aldrich) in PBS for 20 minutes at room temperature, the cells were washed with PBS and blocked in 3% bovine serum albumin (BSA) in PBS for 1 hour at room temperature. Cells were then probed with rabbit polyclonal antibodies against PAI1 (Abcam, ab66705) or CD31 (Abcam, ab28364) overnight at 4°C, followed by labeling with an Alexa Fluor 555 donkey anti-rabbit antibody (Thermo Fisher Scientific, A-31572) or an Alexa Fluor 488 goat anti-rabbit antibody (Thermo Fisher Scientific, A-11034) for 1 hour in the dark at room temperature. For immunostaining of kidney tissues, cryo-sections were air-dried at room temperature, and then fixed in PBS supplemented with 4% paraformaldehyde (Electron Microscopy Sciences) for 20 minutes at room temperature. After permeabilization with 0.3% Triton X-100 in PBS for 20 minutes at room temperature, the sections were blocked in 10% goat serum in PBS at room temperature for 1h, and then incubated with a primary rabbit monoclonal antibody to vimentin (Cell Signaling, 5741) overnight at 4°C. After washing with PBS three times, the sections were labeled with Alexa Fluor 647-conjugated secondary antibody (Cell Signaling, 4414) for 1 hour in the dark at room temperature. Analysis of EndoMT in the renal vasculature was performed by two independent and blinded investigators. Each scored for the co-localization of EndoMT green fluorescent protein (GFP) and vimentin in kidney sections obtained from 1-2-month-old mice by analyzing multiple random fields per animal. There was some degree of subjectivity in this analysis leading to differences between observers in the absolute levels of EndoMT, although both observers noted an approximate 2-fold relative increase in the $Cpt2^{E-KO}$; mTmG mice.

For immunostaining of embryonic tissues, the sections were deparaffinized using the Leica Autostainer XL (Leica Biosystems). After antigen retrieval in citrate buffer (Sigma-Aldrich, C9999) the sections were permeabilized with 0.3% Triton X-100 in PBS for 20 minutes at room temperature, and then blocked in 3% BSA in PBS at room temperature for 1 hour. Immunostaining for GFP was performed using a chicken polyclonal antibody against GFP (Abcam, ab13970, 1:250) incubated overnight at 4°C and followed by an Alexa Fluor 488 AffiniPure donkey anti-chicken secondary antibody (Jackson ImmunoResearch Laboratories, cat no. 703-545-155) incubated for 1 hour at room temperature. For immunostaining of cardiac valve tissues in postnatal mice, cryo-sections were air-dried at room temperature, and then fixed in a 4% paraformaldehyde/PBS solution for 20 minutes at room temperature. After permeabilization with 0.3% Triton X-100 in PBS for 20 minutes at room temperature, the sections were blocked in 10% goat serum in PBS at room temperature for 1h, and then incubated with the Alexa Fluor 647 anti-mouse CD45 antibody (BioLegend, 103124) overnight in the dark at 4°C. For all sections, after washing with PBS three times, DAPI (4',6-diamidino-2-phenylindole) counterstaining was applied for 20 minutes at room temperature before mounting with VECTASHIELD mounting medium (Vector Laboratories). After mounting, all coverslips were sealed with nail polish and images were acquired using an inverted Zeiss LSM 780 Confocal Microscope (Zeiss) equipped with a Plan-Apochromat 40 × /1.4 NA, and 63 × /1.40 NA oil immersion objective lens driven by ZEN software. When comparing the levels of immunostaining, the samples were stained at the same time and the images were acquired using constant microscope capture settings. Images for tissue EndoMT were deconvolved using Huygens software (SVI, Netherlands) and merged tiffs were generated using Imaris software 9.0.2 (Bitplane, Zurich Switzerland). Average fluorescence intensity (AFI) was determined by dividing the overall mean fluorescence intensity by the area of the cell and quantified using MetaMorph Offline software 7.8.12.0 (Molecular Devices). For each group, AFI was calculated from over 50 cells obtained from at least five random 40 × fields.

Real-time qPCR

Total RNAs from cultured human or mouse endothelial cells or mouse homogenized tissues were extracted using the RNeasy Mini Kit (QIAGEN). During RNA purification, DNase digestion was performed using RNase-free DNase Set (QIAGEN). Complementary DNA

Molecular Cell 69, 689–698.e1–e7, February 15, 2018   e5

was prepared using iScript cDNA Synthesis Kit (Bio-Rad). Real-time qPCR was performed on an MxP3005P real-time PCR system (Stratagene) or LightCycler 96 real-time PCR System (Roche) using FastStart Universal SYBR Green Master (Roche) mix according to the manufacturer's instructions. Data were analyzed using the comparative cycling threshold ($\Delta\Delta Ct$) method. Primers were synthesized and purified by Integrated DNA Technologies, and checked for specificity against human Refseq mRNA database using Primer-BLAST (https://www.ncbi.nlm.nih.gov/tools/primer-blast/). The primer sequences used for detection of gene expression are included in Table S2.

Metabolic assays

For metabolomics analysis, HPMVECs were treated with cytokines every other day over a nine-day period and then collected and frozen in liquid nitrogen. Cell media were supplemented with 1mM L-Carnitine hydrochloride (Sigma-Aldrich) 24 hours before the cell harvest. Each group has five replicates, and each replicate has approximate 2×10^6 cells. Samples were collected and stored at $-80°C$ and subsequently analyzed by the Metabolomics Core at the Sanford Burnham Prebys Medical Discovery Institute. A PicoProbe acetyl-CoA fluorometric assay kit (BioVision) and a SpectraMax Gemini EM Microplate Reader (Molecular Devices) were used for measurement of acetyl-CoA levels. For the FAO assay, the XF96 extracellular flux analyzer (Agilent) was used to assess the cell's ability to oxidize exogenous fatty acids. In brief, each well of the Utility Plate was filled with 200 μL XF Calibrant Solution (Agilent) overnight in a humidified non-CO2 37°C incubator. For HPMVECs with or without treatment of TGF-β1 and IL-1β and with or without etomoxir treatment, 4×10^4 human endothelial cells per well were seeded on a fibronectin-coated XF96 cell culture microplate (Agilent) and cells were then incubated in substrate-limited medium (2.5 mM glucose, 1.0 mM GlutaMax, 0.5 mM carnitine, 1% FBS, EGM-2 MV SingleQuots Kit and DMEM without glucose, glutamine, or HEPES) for 4 hours. For control or $Cpt2^{E-KO}$ derived endothelial cells, 2×10^4 mouse endothelial cells per well were cultured overnight in a fibronectin-, gelatin- and collagen-coated XF96 cell culture microplate (Agilent). Immediately before the assay for either human or mouse endothelial cells, the medium was changed to FAO assay medium (111 mM NaCl, 4.7 mM KCl, 1.25 mM CaCl2, 2.0 mM MgSO4, 1.2 mM Na2HPO4, 2.5 mM glucose, 0.5 mM carnitine and 5 mM HEPES), adjusted to pH 7.4, and cells were subsequently maintained in a non-CO2 incubator for 45-60 minutes at 37°C. The XF Palmitate-BSA FAO Substrates (Agilent) palmitate-BSA (166.7 μM palmitate conjugated with 28.3 mM BSA) or BSA (28.3 mM BSA) was then added, and the oxygen-consumption rate (OCR) was analyzed employing the XF Cell Mito Stress Test using Wave software (Agilent). For analysis of OCR with CPT1A overexpression in HPMVECs with or without treatment of TGF-β1 and IL-1β, 4×10^4 human endothelial cells per well were seeded on a fibronectin-coated XF96 cell culture microplate (Agilent) and cells were then incubated in full medium for 4 hours. Immediately before the assay, the medium was changed to cell mito stress test assay medium (XF Base Medium with 2.5 mM glucose, 1 mM pyruvate and 1 mM glutamine), adjusted to pH 7.4, and cells were subsequently maintained in a non-CO2 incubator for 1 hour at 37°C.

Palmitate oxidation rate assay

Palmitate oxidation was measured as previously described (Huynh et al., 2014) with minor modifications. Briefly, HPMVECs were plated in 6-well plates with or without three or four days' treatment of TGF-β1 and IL-1β. On the day of the experiment, growth medium was substituted for reaction media containing 0.7% fatty acid-free BSA (Sigma-Aldrich, Cat#A9205), 0.3mM cold palmitate (Sigma-Aldrich, Cat#P9767), 2 μCi ml^{-1} 1-^{14}C-palmitate (PerkinElmer, Cat#NEC075H050UC), 1mM carnitine (Sigma-Aldrich, Cat#C0283), and supplemented with 1.5g/L sodium bicarbonate (Sigma-Aldrich, Cat#792519). Cells were incubated in reaction media for 3 hours at 37°C, after which media and cells were collected for analysis. The rate of palmitate oxidation was calculated using the measured $^{14}CO_2$ released into the media and specific activity of 1-^{14}C-palmitate in the reaction media, corrected to total protein.

Cardiac valve analysis

For analysis of valve thickness, 1-2-month-old male and female mice were euthanized and the hearts were collected, fixed for 24 hours in 10% neutral buffered formalin fixative (Azer Scientific), and then embedded in paraffin. The valves in paraffin-embedded hearts were completely sectioned into 5 μm thick sections and stained with hematoxylin and eosin (H&E) using the Leica Autostainer XL (Leica Biosystems). H&E-stained slides were imaged on a NanoZoomer 2.0-RS Digital slide scanner (Hamamatsu Photonics) and analyzed using NDP view2 software (Hamamatsu Photonics). Approximately 20 sections were obtained for each valve and the image with the maximum thickness for each animal was quantified. The anterior leaflet of the mitral valve was analyzed because it was the easiest valvular structure to unambiguously assess histologically. The observer was blinded to the genotype of the animal for the analysis. For EndoMT lineage tracing using the dual reporter embryos, embryos were harvested at approximately embryonic day E17.5, fixed overnight in 10% neutral buffered formalin fixative (Azer Scientific), and then embedded in paraffin. The valves of these paraffin-embedded embryos were completely sectioned into 5 μm thick sections. Following this, the sections were processed for GFP immunostaining. For lineage tracing using the dual reporter in postnatal mice, tissues were embedded in Tissue-Tek OCT (Sakura) and snap frozen. Ten-micrometer-thick frozen sections were subsequently fixed in 4% paraformaldehyde (Electron Microscopy Sciences), counterstained with DAPI, mounted with VECTASHIELD medium (Vector Laboratories) and then subjected to fluorescence microscopy analysis using an inverted Zeiss LSM 780 Confocal Microscope (Zeiss) driven by ZEN software. Approximately 10 images per valve were obtained and the portion with the maximum number of GFP positive interstitial cells analyzed. The observer was blinded to the genotype of the animal for the quantification. In addition, CD45 immunostaining was performed to confirm that valvular GFP-positive cells represented endothelial cells and not a hematopoietic (CD45$^+$) cell population.

Cell growth assay

A tetrazolium dye 3-(4,5-dimethylthiazol-2-yl)-2,5-diphenyltetrazolium bromide (MTT)-based colorimetric kit (Millipore, CT02) was used for determination of growth rates of mouse endothelial cells. Four thousand cells per well were seeded into 96-well microplate. At the end of assay, the cells were treated with 10 μL of a MTT solution and then incubated at 37°C for an additional 5 hours. After addition of 0.1 mL of isopropanol (Sigma-Aldrich) with 0.04 N HCl to each well, MTT formazan was added, mixed thoroughly, and then the absorbance at 570 nm measured using a SpectraMax Plus 384 Microplate Reader (Molecular Devices). The data was analyzed using SoftMax Pro software (version 7.0).

High-performance liquid chromatography (HPLC) analysis of malonyl-CoA

After collection, HPMVECs with or without two days' treatment of TGF-β1 and IL-1β, were resuspended in 5% of 5-sulfosalicylic acid (Sigma-Aldrich) solution. To permeabilize the cells, samples were frozen in liquid nitrogen and thawed on ice for two times. After centrifugation, the supernatant was filtered using Ultrafree-MC LH Centrifugal Filter (Millipore, Cat#UFC30LH25). Then, the samples were transferred into SUN-SRi Glass Microsampling Vials (Thermo Fisher Scientific, Cat#14-823-359) with SUN-SRi 11mm Snap Caps (Thermo Fisher Scientific, Cat#14-823-379). Malonyl-CoA was separated using an Agilent 1100 HPLC with Fluorescence detector (Agilent) on a Luna 3 μm C18(2) column (150x4.6mm, 3 μm, Phenomenex, Torrance, CA). Quantification of malonyl-CoA was performed by the ChemoStation software Rev. A.10.01 (Agilent), monitoring 259 nm as the maximum absorbance for malonyl-CoA.

Determination of endothelial permeability

Blood vessel permeability assay was performed according to a previous protocol with some minor modifications (Radu and Chernoff, 2013). In brief, awake and restrained mice received intravenous tail injection of 2% sterile solution of Evans Blue (J. T. Baker Chemicals) in PBS (4 mL kg^{-1}). After thirty minutes when assessing lung permeability (6-13-week-old female mice), or on the following day for kidney and spleen permeability analysis (5-11-week-old male animals), mice were perfused with a solution of PBS containing 10 U ml^{-1} heparin (Sigma-Aldrich) using a Masterflex C/L Tubing Pump (Cole-Parmer Instrument). After perfusion, the tissues were quickly removed and placed into formamide at 55°C for 48 hours for tissue extraction of Evans Blue. The level of Evans Blue extravasation was quantified by measuring absorbance at 610 nm and then normalized to the initial amount of organ weight (mg tissue). The permeability analysis was performed in a blinded fashion.

Analysis of genetic variants

The study population was developed from the BioVU biorepository, a Vanderbilt University Medical Center resource linking over 215,000 DNA samples to a de-identified electronic health record (EHR). The development of BioVU has been described previously (Roden et al., 2008). At the time of this study, approximately 32,000 samples had been genotyped using the Illumina HumanExome BeadChip v.1.0 (exome chip) as part of ongoing research efforts. This platform contains ~250,000 rare and common coding SNPs (https://genome.sph.umich.edu/wiki/Exome_Chip_Design), including (after quality control) 8 missense variants in CPT1A (Missense: T101M, A275T, R284H, R288Q, P510L, V626L, N733S and V54L) and 15 in CPT2 (Missense: M647V, E545A, V533A, G480R, K458Q, F352C, R350C, M342T, N311S, P284S, R167Q, D118G, S113L, A101V and K79T). Clinically diagnosed CKD was defined as the presence of 1 or more 585* International Classification of Diseases, Ninth Revision, Clinical Modification (ICD-9-CM) codes. Phenotypes included in BioVU Illumina HumanExome BeadChip v.1.0 cohort are as follows: (1) Drug response/toxicity phenotypes; (2) Longitudinal cohorts of subjects with ≥ 3 years of follow-up; (3) Elderly (> 75 years); (4) Pediatric populations; (5) The Vanderbilt Tumor Registry of subjects with cancer (melanoma, GI, head and neck, brain, thyroid, gynecologic, lung, prostate, or breast cancer); (6) Rare diseases as defined by the U.S. Food and Drug Administration (FDA). Samples were genotyped using the Illumina HumanExome BeadChip v.1.0 that contains ~250,000 rare and common coding SNPs (https://genome.sph.umich.edu/wiki/Exome_Chip_Design). Quality control parameters were applied at the sample (call rate < 95%, sex discrepancy, unexpected relatedness, duplicate concordance, and HapMap concordance) and SNP level (call rate < 95%, replicate concordance, Mendelian errors). In total, 242,901 SNPs passed quality control metrics and were included in the analysis. Analyses included all white subjects with exome chip genotyping data. Association between variants and CKD was assessed using multivariable logistic regression adjusting for age, gender, diabetes status, and hypertension status. The threshold for statistical significance was set at $p = 0.002$ using a Bonferroni-adjustment based on the total number of variants tested (0.05/30).

QUANTIFICATION AND STATISTICAL ANALYSIS

The statistical significance of differences between groups was evaluated by unpaired two-tailed Student's t test unless mentioned otherwise. For bar graphs, results are represented as the mean ± standard error of the mean (SEM). p values < 0.05 were considered significant. GraphPad Prism version 7.02 software was used for statistical calculations. Blinded analyses were performed for Figures 4F, 4J, 4K, and S4I. No statistical methods were used to predetermine sample size.

DATA AND SOFTWARE AVAILABILITY

Software is listed in the Key Resources Table.